

Epitaxial growth of ultraflat stanene with topological band inversion

Jialiang Deng^{1,7}, Bingyu Xia^{2,3,7}, Xiaochuan Ma^{1,7}, Haoqi Chen¹, Huan Shan¹, Xiaofang Zhai¹, Bin Li¹, Aidi Zhao^{1*}, Yong Xu^{2,3,4*}, Wenhui Duan^{2,3,5}, Shou-Cheng Zhang⁶, Bing Wang^{1*} and J.G.Hou¹

Two-dimensional (2D) topological materials, including quantum spin/anomalous Hall insulators, have attracted intense research efforts owing to their promise for applications ranging from low-power electronics and high-performance thermoelectrics to fault-tolerant quantum computation. One key challenge is to fabricate topological materials with a large energy gap for room-temperature use. Stanene—the tin counterpart of graphene—is a promising material candidate distinguished by its tunable topological states and sizeable bandgap. Recent experiments have successfully fabricated stanene, but none of them have yet observed topological states. Here we demonstrate the growth of high-quality stanene on Cu(111) by low-temperature molecular beam epitaxy. Importantly, we discovered an unusually ultraflat stanene showing an in-plane s - p band inversion together with a spin-orbit-coupling-induced topological gap (~ 0.3 eV) at the Γ point, which represents a foremost group-IV ultraflat graphene-like material displaying topological features in experiment. The finding of ultraflat stanene opens opportunities for exploring two-dimensional topological physics and device applications.

Two-dimensional (2D) topological materials, including quantum spin Hall (QSH) and quantum anomalous Hall (QAH) insulators, are intriguing emergent states of quantum matter characterized by a nontrivial band topology and topologically protected metallic edge states, which are useful for realizing dissipationless conduction, magnetic monopoles, Majorana fermions, and so on¹⁻⁷. Various 2D topological materials have recently been theoretically proposed and investigated⁸⁻²², but very few have been experimentally fabricated and confirmed to be topologically nontrivial. Among them, one promising material candidate is stanene¹⁰, which is theoretically predicted to be the latest cousin of graphene, composed of an atomic layer of tin (Sn) in a low-buckled honeycomb lattice. Benefitting from the heavy element and structural buckling, stanene has strong spin-orbit coupling (SOC) and shows extraordinarily large QSH and QAH gaps (~ 0.3 eV), feasible for room-temperature applications^{10,23}. Moreover, the topological states of stanene are highly tunable and can be varied from π to σ orbitals by chemical functionalization. Thus, the two classical models (that is, the Kane–Mele⁸ and Bernevig–Hughes–Zhang³ models) can both be studied in stanene, offering an ideal platform to explore 2D topological physics^{12,24,25}. The intriguing proposals have stimulated intensive experimental efforts. In 2015, monolayer (ML) stanene was successfully fabricated on Bi₂Te₃(111), confirming the existence of the theoretically predicted structure¹⁷. Further experiments on different substrates obtained ML stanene with distinct material properties²⁶⁻³⁰. However, none of the experiments reported the finding of topological states in stanene, due to unfavourable substrate effects. Very recently, superconductivity was discovered in few-layer stanene, offering opportunities to explore Majorana fermions³¹. A critical issue is to grow stanene with topologically nontrivial states, which requires accurate

control over substrate/interface structures at the atomic level and still remains elusive.

In this work, we grew Sn films on Cu(111) by molecular beam epitaxy (MBE) and measured the atomic and electronic structures by scanning tunnelling microscopy (STM) and angle-resolved photoemission spectroscopy (ARPES) for comparison with first-principles calculations. Unexpectedly, we obtained high-quality ML stanene samples crystallized in an unusually ultraflat honeycomb lattice, although structural buckling is well known to be a key ingredient to lower the free energy and a planar stanene is believed to be unstable. Further analysis shows that the substrate not only stabilizes the ultraflat structure, but also causes significant lattice stretching and orbital filtering effects in stanene. These substrate effects synergistically generate an ultraflat stanene with an s - p band inversion together with a sizeable SOC-induced gap (~ 0.3 eV), giving topologically derived edge states within the energy gap. Our finding of ultraflat stanene sheds light on future research and applications of planar graphene-like materials.

The schematic sample preparation set-up is shown in Fig. 1a. Sn atoms were evaporated from an effusion cell onto a Cu(111) surface held at ~ 200 K in ultrahigh vacuum. The samples were then cooled to 5 K for STM and scanning tunneling spectroscopy (STS) measurements without annealing (see Methods). Figure 1b shows a representative STM topographic image of a 0.9 ML sample. Most of substrate is covered by uniform continuous Sn film except a few small regions of bare substrate, which clearly reflects a typical 2D growth mode. The apparent height of the Sn film is 0.18 nm (Fig. 1b), indicating it is a single atomic layer in thickness. The detailed atomic network is visualized in Fig. 1c, mimicking a well-known graphene structure but with a much larger lattice constant of 0.51 nm, which is exactly twice that of the underlying Cu(111)

¹Hefei National Laboratory for Physical Sciences at the Microscale and Synergetic Innovation Center of Quantum Information & Quantum Physics, University of Science and Technology of China, Hefei, China. ²State Key Laboratory of Low Dimensional Quantum Physics, Department of Physics, Tsinghua University, Beijing, China. ³Collaborative Innovation Center of Quantum Matter, Beijing, China. ⁴RIKEN Center for Emergent Matter Science (CEMS), Wako, Japan. ⁵Institute for Advanced Study, Tsinghua University, Beijing, China. ⁶Stanford Center for Topological Quantum Physics, Stanford University, Stanford, CA, USA. ⁷These authors contribute equally: Jialiang Deng, Bingyu Xia, Xiaochuan Ma. *e-mail: adzhao@ustc.edu.cn; yongxu@mail.tsinghua.edu.cn; bwang@ustc.edu.cn

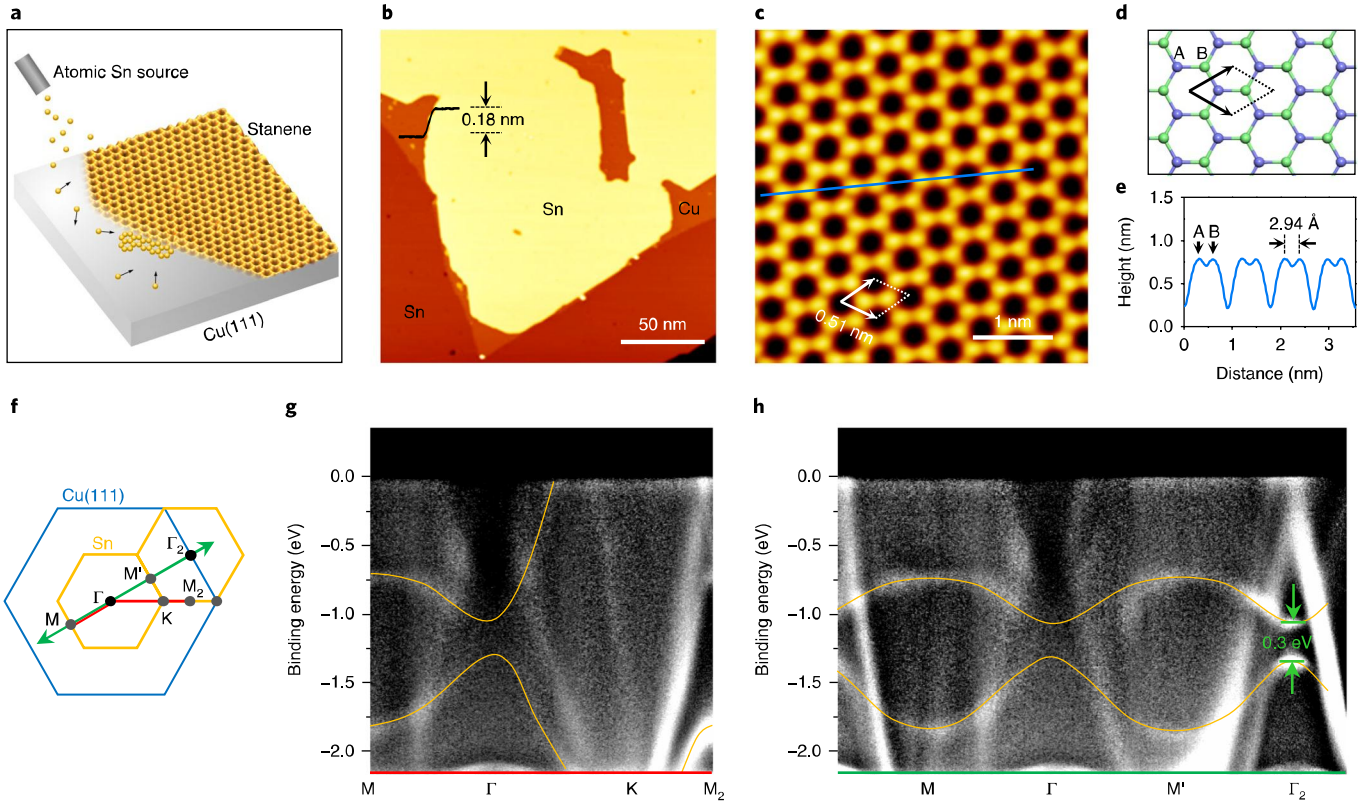


Fig. 1 | Atomic and electronic structures of ultraflat stanene on Cu(111). **a**, Schematic sample preparation set-up. **b**, STM image of Sn deposited on Cu(111) with 0.9 ML coverage (sample bias $V_s = -1$ V, tunnelling current $I = 0.1$ nA). **c**, High-resolution STM image of the stanene film ($V_s = 1$ V, $I = 0.4$ nA). **d**, Schematic atomic model of the honeycomb stanene in **c**. **e**, Profile along the line in **c** showing that the adjacent Sn atoms are identical in apparent height. **f**, 2D BZs of ultraflat stanene on Cu(111). The second BZ of stanene is also shown. **g,h**, ARPES spectra of 0.9 ML stanene on Cu(111) along the M- Γ -K- M_2 (red line in **f**) (**g**) and M- Γ -M'- Γ_2 (green line in **f**) (**h**) directions. The orange lines outline the energy bands which are contributed mainly by orbitals of Sn.

surface (2.55 Å). Considering the relative orientation between the Sn film and the substrate, the honeycomb structure can be viewed as a (2×2) superstructure. The most intriguing fact is that this honeycomb lattice is completely flat, as illustrated in Fig. 1d,e. There are two nonequivalent Sn atoms in a unit cell (Fig. 1d). In the height profile along the blue line (Fig. 1e), the two adjacent Sn atoms are clearly resolved and identical in height. The Sn-Sn bond length in this honeycomb structure is 2.94 Å, close to the bond length of 2.81 Å in bulk α -Sn and 2.83 Å in freestanding stanene¹⁰. Our STM results clearly show that an atomic layer of Sn in a planar honeycomb lattice with zero structural buckling, namely ultraflat stanene, is formed on Cu(111).

Such an unexpected ultraflat stanene inspires us to look further into its electronic structure. The high uniformity of the ultraflat stanene grown on Cu(111) enables high-resolution ARPES measurements. The stanene/Cu(111) surface Brillouin zones (BZs) are shown in Fig. 1f. The ARPES spectra of 0.9 ML stanene along M- Γ -K- M_2 are presented in Fig. 1g. Here M_2 is the M point of the second BZ. The ARPES spectra show additional fine features in comparison with those of clean Cu(111), which are marked by orange lines and can be ascribed to the presence of stanene (Supplementary Fig. 1). It is found that the experimental band structure shows an obvious gap between two intense bands centred at the Γ point. The bandgap opening can be more clearly visualized at the Γ_2 point in the second BZ, which is equivalent to the Γ point of the first BZ. Figure 1h shows the ARPES spectra along a cut in the M- Γ -M'- Γ_2 direction. A remarkable gap opening with an amplitude of ~ 0.3 eV centred at around -1.25 eV is clearly resolved. Interestingly, we

found that such a band structure as well the noticeable gap opening at the Γ point present significant similarities to the p_{xy} orbitals and large SOC gap predicted for fluorinated stanene despite the energy difference¹⁰, implying a possible similar mechanism for the ultraflat stanene.

2D Xenes (X=Si, Ge, Sn) all have buckled honeycomb structures due to their weak π bonds, thus π - σ interactions are allowed by buckling, leading to a more stabilized structure than the planar one. This is well established both theoretically and experimentally¹². Previous experiments on stanene mostly obtained low-buckled structures²⁶⁻²⁹. Nearly planar stanene with low height variations was obtained only on Ag(111) with a Ag-Sn surface alloy³⁰. The growth of ultraflat stanene with zero height variation in the present experiment seems contradictory to common sense. Something unusual must happen to explain our experimental finding. We performed first-principles calculations to reveal the underlying mechanism (Fig. 2). Generally one would expect a smaller buckling (δ) in a stretched lattice. For a freestanding stanene, δ decreases from 0.85 Å to 0.72 Å by varying the lattice constant (a) from 4.68 Å (a_0) to 5.1 Å. Obviously, the lattice stretching itself is not enough to explain the experiment results. In fact, a freestanding stanene with zero buckling is unstable (Fig. 2c), implying an indispensable role for the substrate. Once including a substrate, both the energy of stanene itself (E_1) and the energy contributed through interactions with the substrate (E_2) should be taken into account. When forcing $\delta = 0$ Å, E_1 increases by 0.19 eV. The dominant energy contribution comes from E_2 , considering that the adsorption energy of stanene is ~ 1.16 eV/atom on Cu(111). By reducing buckling, all

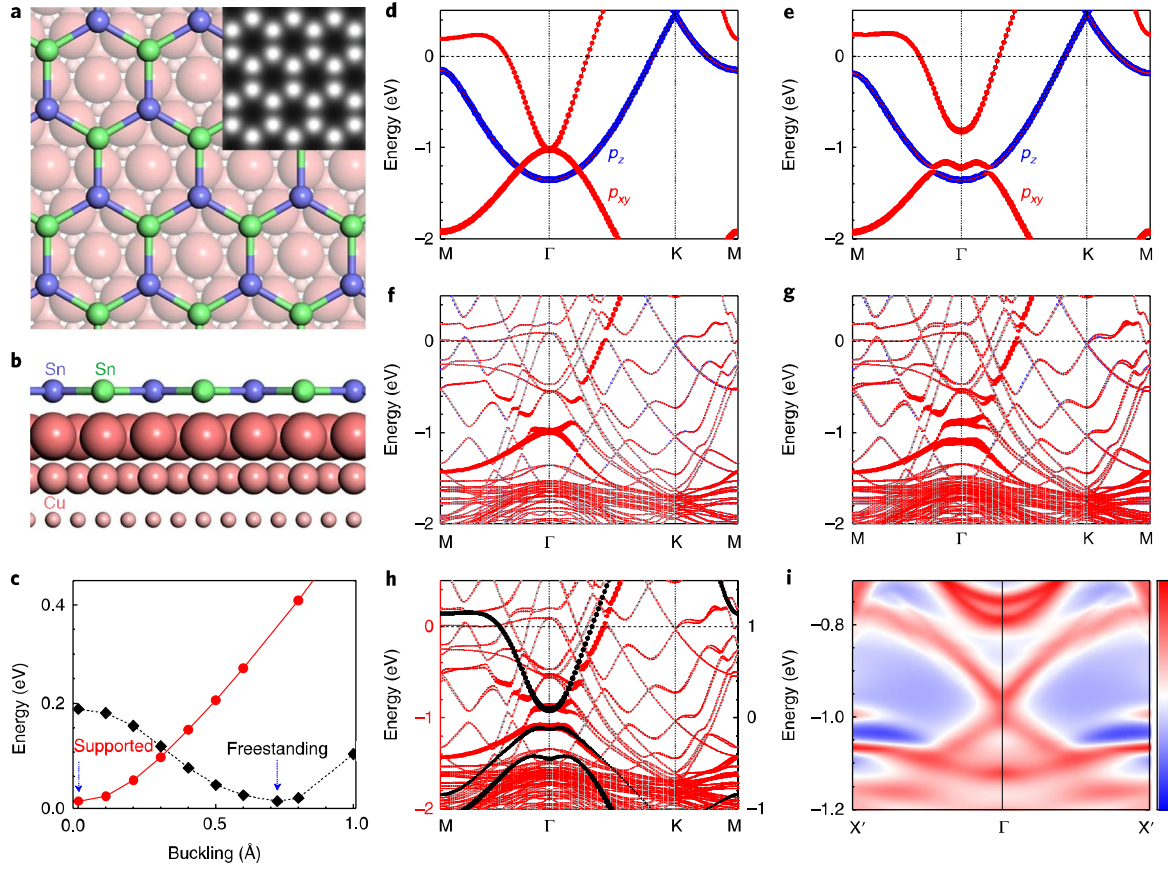


Fig. 2 | Calculated atomic and electronic structures of the ultraflat stanene. **a,b**, Crystal structure for stanene on Cu(111) from the top (**a**) and side (**b**) views. Inset, corresponding theoretically simulated STM image. **c**, Energy as a function of buckling for freestanding and supported stanene, referenced to the minimal energy. **d-g**, Band structures for freestanding (**d,e**) and supported (**f,g**) stanene excluding (**d,f**) and including (**e,g**) the SOC. Red (blue) dots denote the contribution from the p_{xy} (p_z) orbital of Sn. **h**, Same as **g**, together with the band structure of a freestanding hydrogenated stanene (black). **i**, Edge states for semi-infinite stanene/Cu(111) with a zigzag-type termination, showing linearly dispersing Dirac-like bands within the SOC-induced gap (approximately -1.0 eV) near the Γ point. $X' = 0.1\pi/L_0$, where L_0 is the lattice periodicity. A high (low) density of states is coloured red (blue).

the Sn atoms of stanene are able to couple strongly with the substrate, which reduces E_2 considerably. Thus a net energy gain is obtained by minimizing δ , and zero buckling corresponds to the most stable geometry (Fig. 2c). Moreover, the theoretically predicted ultraflat geometry of stanene/Cu(111) agrees well with STM measurements. In the most stable configuration (Fig. 2a,b), the adsorption height is 2.36 \AA , which is comparable to the apparent height of 1.8 \AA measured by STM (Fig. 1b). Each stanene unit cell is adsorbed on a 2×2 Cu(111) supercell, in which one Sn atom is on the hexagonal close-packed hollow site and the other on the face-centred cubic hollow site, exactly the same as experimentally observed (Supplementary Fig. 2). It is worth noting that both the sublattice Sn atoms of stanene are located at hollow sites and have essentially the same chemical environments, making the ultraflat stanene a true analogue of graphene where the two sublattice atoms are chemically indistinguishable.

For comparisons, on PbTe(111) (ref. 27), which can form chemical bonds with only half the Sn atoms of stanene, E_2 would increase considerably if a planar structure was enforced. On the weakly bonded substrate $\text{Bi}_2\text{Te}_3(111)$ (ref. 17), the energy contribution is dominated by E_1 , that prefers a finite buckling as well. Therefore, the interplay of the energies (E_1 and E_2) and structural buckling determines whether a planar configuration is stable or not. The revealed mechanism could be applied to design further planar graphene-like structures of other materials.

Previous work found that an s - p band inversion could happen at the Γ point in the condition of large lattice constants, which induces a topological phase transition in stanene^{10,25}. However, none of the existing stanene samples show this band inversion, since most of them have a lattice constant compressed by substrates ($a = 4.38 \text{ \AA}$ on $\text{Bi}_2\text{Te}_3(111)$ (ref. 17) and $a \sim 4.52 \text{ \AA}$ on $\text{PbTe}(111)$ (ref. 27)). Intriguingly, a tensile strain is applied to stanene on Cu(111) and the lattice constant is greatly enlarged to 5.1 \AA . To see the strain effect, we computed the band structure for a freestanding ultraflat stanene (Fig. 2d,e). The p_{xy} bonding states are located far above the s antibonding states at the Γ point (Supplementary Fig. 3), showing an inverted band order. When excluding the SOC, the p_{xy} orbitals are degenerate at the Γ point. They are decoupled from the p_z orbitals due to the ultraflat geometry, and the corresponding bands cross each other along Γ -K and Γ -M (Fig. 2d). When including the SOC, avoided crossings appear between bands contributed by p_{xy} and p_z . More importantly, a bandgap ~ 0.40 eV is opened at the Γ point for the p_{xy} orbitals. This SOC-induced gap is interesting from the topological point view, as we will discuss below.

When taking the substrate into account, the p_z orbitals of stanene are strongly hybridized and become indistinguishable from substrate states, whereas the p_{xy} orbitals remain predominantly unaffected and can be clearly visualized by orbital projection (Fig. 2f). The SOC-induced gap at the Γ point still exists, but the gap value decreases to ~ 0.22 eV as a result of the weakened SOC on the

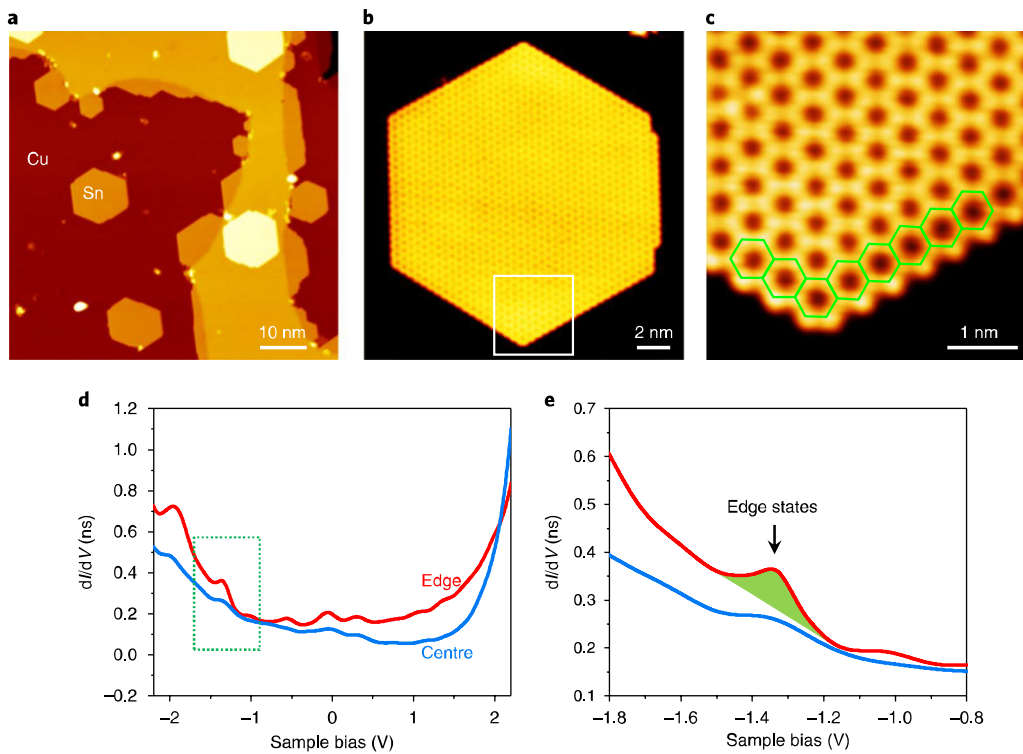


Fig. 3 | Edge structure and edge states of the ultraflat stanene flakes. **a**, STM image ($V_s = -0.5$ V, $I = 0.1$ nA) of Sn deposited on Cu(111) with 0.2 ML coverage. **b**, Representative stanene flake with a hexagonal shape. **c**, Zoom-in STM image ($V_s = -0.5$ V, $I = 0.6$ nA) of the white square in **b**, showing the zig-zag type edge. **d**, dI/dV spectra taken at the edge and centre of the stanene flakes. **e**, Zoom-in dI/dV spectra indicated by the green dashed rectangle in **d** to highlight the differences. The enhanced spectral weight located between -1.2 V and -1.45 V is attributed to the edge states.

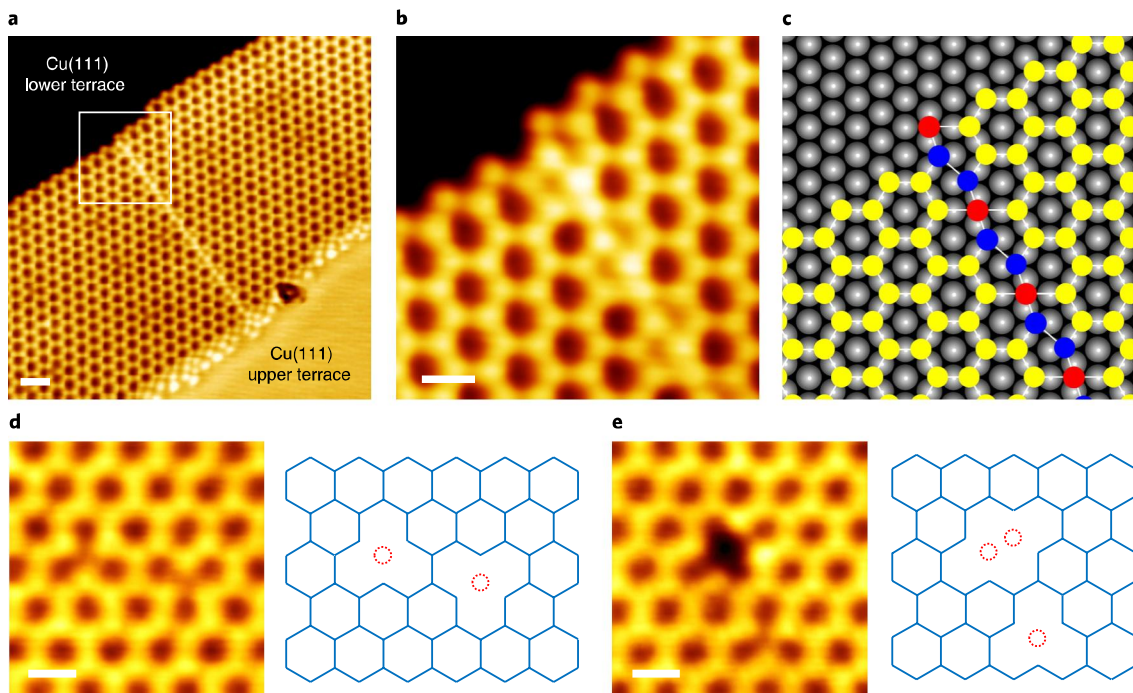


Fig. 4 | Atomically resolved line defect and point defects in the ultraflat stanene. **a**, STM image ($V_s = 0.5$ V, $I = 0.6$ nA) of a stanene domain boundary (line defect) close to a Cu(111) step. Scale bar, 1 nm. **b**, Zoom-in STM image of **a** gives the detailed boundary structure. Scale bar, 0.5 nm. **c**, Atomic stacking model for **b**, which reveals both the lattice mismatch between domains and adsorption sites of Sn atoms. Each unit in the boundary has a Sn atom with four-fold coordination, which has not been observed for graphene boundaries. **d,e**, Atomically resolved STM images of two typical point defects: monovacancy (**d**) and divacancy (**e**). Scale bars, 0.5 nm.

substrate (Fig. 2g). In this sense, the Cu(111) substrate can be viewed as an 'orbital filter'³², which selectively filters out the p_z orbitals of stanene. Thus the epitaxial stanene can be viewed as a honeycomb lattice of in-plane p_{xy} orbitals, which is of great interest in topological physics^{33,34}. By comparing the calculated band diagram with the ARPES spectra (Fig. 1g,h), we found that the topological gap is approximately -1.0 eV in theory, slightly higher than the experimental value of approximately -1.25 eV. This quantitative discrepancy is explained by the inaccurate description of Cu d -bands (higher in energy than experiment), caused by the generalized gradient approximation used in the density functional theory calculations. Despite the minor discrepancy, we found excellent agreement between experiment and theory in both the band dispersion and gap opening, strongly suggesting the band inversion and SOC as the origins of the gap at the Γ point.

A recent work reported the epitaxial growth of a nearly planar stanene over a Ag–Sn surface alloy on Ag(111)³⁰, which also shows an enlarged lattice constant (~ 5.0 Å) and thus might give a topological band inversion. However, as the Ag–Sn surface alloy shows slight structural corrugation and the two sublattice Sn atoms of stanene are located at different surface sites with significantly distinct chemical environments (one above Ag–Ag and the other above Ag–Sn), their stanene sample exhibits a finite structural buckling. Moreover, due to the complicated mixing between the surface Sn and subsurface Sn layers, it becomes challenging to characterize the band features of stanene separately. Whether their material sample exhibits topological band features or not remains unknown.

The multi-orbital honeycomb has been theoretically revealed to be topologically nontrivial³². Although the band topology is not well defined for gapless states, topologically derived boundary states (TDBSs) could appear within an inverted energy gap, as experimentally found for noble metal surfaces³⁵. Similarly, based on the s – p band inversion, one would expect TDBSs within the SOC-induced gap of stanene/Cu(111). Despite the unwanted metallic states from the substrate, our Green's function calculation clearly shows linearly dispersing Dirac-like edge bands within the SOC-induced gap near the Γ point (Fig. 2i), confirming the existence of TDBSs. The topological feature can be further clarified by considering an equivalent system—a hydrogenated stanene (that is stanane), whose p_z orbitals are removed from the Fermi level by hydrogenation, giving a p_{xy} -orbital honeycomb as well. The ultraflat stanane shows essentially the same p_{xy} -derived bands and SOC-induced gap around the Γ point (Fig. 2h), which confirms the equivalence of the two systems. We calculated the band structure for a nanoribbon of ultraflat stanane (Supplementary Fig. 4), which also shows TDBSs within the SOC-induced gap.

As a direct consequence of band inversion and the opening of a SOC-induced gap, TDBSs within the energy gap are expected to exist at the edges of stanene. Since the sample is nearly fully covered with stanene, it is not accessible for ARPES measurements to detect the in-gap edge states. To verify the existence of the TDBSs, submonolayer ultraflat stanene was grown (Fig. 3) and subjected to STS measurements. The ultraflat honeycomb structure of stanene resolved with single-atomic precision allows the direct observation of a variety of topological structures, including edge termination and defect structures (see Fig. 4 for typical line and point defects). Structural determination of these features at the single-atomic level in graphene and graphene-like 2D materials is highly challenging and of crucial importance because it refers directly to many exotic properties^{36–40}. As a predominant analogue of graphene in an ultraflat honeycomb structure, the stanene flakes are expected to bear a great resemblance to graphene in edge structures, defects and chemical stability. In our case, the stanene flakes we observed are mostly zigzag-terminated (Fig. 3c), in accordance with graphene. The TDBSs should introduce an increased density of states within the energy window of the SOC-induced gap, which can be observed

as an enhancement in the differential conductance spectra taken at the edges. Figure 3d,e shows typical spectra for a hexagonal stanene nanoflake with a diameter of ~ 6 nm. Comparing the two dI/dV spectra taken at the edge and centre of the flake, we indeed found a pronounced peak developed in the energy range from -1.2 V to -1.45 V, in line with the energy of the SOC-induced gap (-1.25 eV \pm 0.15 eV) observed in the ARPES results. These edge states can be observed only within a 5-Å-wide rim along the edges (Supplementary Fig. 5), supporting the existence of TDBSs.

To check the stability of the ultraflat stanene, we exposed the sample to oxygen. The main results are shown in Supplementary Fig. 6. After exposure to ~ 100 langmuir oxygen for 10 min, the inner honeycomb structure of ultraflat stanene remains intact. Hence the ultraflat stanene flakes are fairly chemically inert, in contrast to the buckled stanene on PbTe(111) (ref.²⁷), further supporting that the chemically active p_z orbitals are fully 'filtered' via hybridization with the underlying Cu(111) substrate. We expect such a chemical stability may facilitate further transport investigations of stanene, as implemented in the silicene field-effect transistors⁴¹. Concerning thermal stability, the ultraflat stanene on Cu(111) is stable up to ~ 243 K, which is much higher than the temperature of liquid nitrogen (~ 77 K), enabling low-cost practical research and applications.

In summary, 2D high-quality ultraflat stanene is fabricated on Cu(111) by low-temperature MBE, which represents a group-IV analogue of graphene in an ultraflat configuration. The lattice stretching and strong substrate interactions synergistically stabilize the zero-buckling geometry, creating a honeycomb lattice of p_{xy} orbitals by the substrate orbital filtering effect. This multi-orbital honeycomb is characterized by an s – p band inversion and a SOC-induced bandgap at the Γ point, which offers a monolayer stanene sample showing topologically nontrivial features, like the TDBSs. Furthermore, the epitaxial stanene with TDBSs could possibly be a candidate material to explore 2D superconductivity or even Majorana fermions, in light of the recent discovery of superconductivity in ultrathin stanene films³¹. In addition, our first-principles calculations predict that ultraflat germanene and plumbene (monolayer lead) could also be fabricated on Cu(111), which also show an s – p band inversion together with a SOC-induced gap at the Γ point (Supplementary Figs. 7,8). The ultraflat two-dimensional Xene materials (X=Ge, Sn and Pb), including germanene, stanene and plumbene, form a distinct class of ultraflat graphene-like materials that are stabilized by a substrate. An extended discussion of the calculated results can be found in the Supplementary Information. In this context, our work could stimulate future research on finding further ultraflat graphene-like materials with which to investigate low-dimensional and topology-related physics and applications.

Online content

Any methods, additional references, Nature Research reporting summaries, source data, statements of data availability and associated accession codes are available at <https://doi.org/10.1038/s41563-018-0203-5>.

Received: 22 May 2018; Accepted: 18 September 2018;

Published online: 5 November 2018

References

- Hasan, M. Z. & Kane, C. L. Colloquium: Topological insulators. *Rev. Mod. Phys.* **82**, 3045–3067 (2010).
- Qi, X. L. & Zhang, S. C. Topological insulators and superconductors. *Rev. Mod. Phys.* **83**, 1057–1110 (2011).
- Bernevig, B. A., Hughes, T. L. & Zhang, S. C. Quantum spin Hall effect and topological phase transition in HgTe quantum wells. *Science* **314**, 1757–1761 (2006).
- König, M. et al. Quantum spin Hall insulator state in HgTe quantum wells. *Science* **318**, 766–770 (2007).
- Liu, C., Hughes, T. L., Qi, X. L., Wang, K. & Zhang, S. C. Quantum spin Hall effect in inverted type-II semiconductors. *Phys. Rev. Lett.* **100**, 236601 (2008).

6. Knez, I., Du, R. R. & Sullivan, G. Evidence for helical edge modes in inverted InAs/GaSb quantum wells. *Phys. Rev. Lett.* **107**, 136603 (2011).
7. Chang, C. Z. et al. Experimental observation of the quantum anomalous Hall effect in a magnetic topological insulator. *Science* **340**, 167–170 (2013).
8. Kane, C. L. & Mele, E. J. Quantum spin Hall effect in graphene. *Phys. Rev. Lett.* **95**, 226801 (2005).
9. Liu, C. C., Feng, W. X. & Yao, Y. G. Quantum spin Hall effect in silicene and two-dimensional germanium. *Phys. Rev. Lett.* **107**, 076802 (2011).
10. Xu, Y. et al. Large-gap quantum spin Hall insulators in tin films. *Phys. Rev. Lett.* **111**, 136804 (2013).
11. Qian, X. F., Liu, J. W., Fu, L. & Li, J. Quantum spin Hall effect in two-dimensional transition metal dichalcogenides. *Science* **346**, 1344–1347 (2014).
12. Molle, A. et al. Buckled two-dimensional Xene sheets. *Nat. Mater.* **16**, 163–169 (2017).
13. Vogt, P. et al. Silicene: compelling experimental evidence for graphenelike two-dimensional silicon. *Phys. Rev. Lett.* **108**, 155501 (2012).
14. Feng, B. J. et al. Evidence of silicene in honeycomb structures of silicon on Ag(111). *Nano. Lett.* **12**, 3507–3511 (2012).
15. Dávila, M. E., Xian, L., Cahangirov, S., Rubio, A. & Le Lay, G. Germanene: a novel two-dimensional germanium allotrope akin to graphene and silicene. *New J. Phys.* **16**, 095002 (2014).
16. Li, L. F. et al. Buckled germanene formation on Pt(111). *Adv. Mater.* **26**, 4820–4824 (2014).
17. Zhu, F. F. et al. Epitaxial growth of two-dimensional stanene. *Nat. Mater.* **14**, 1020–1025 (2015).
18. Liu, Z. et al. Stable nontrivial Z_2 topology in ultrathin Bi (111) films: A first-principles study. *Phys. Rev. Lett.* **107**, 136805 (2011).
19. Reis, F. et al. Bismuthene on a SiC substrate: A candidate for a high-temperature quantum spin Hall material. *Science* **357**, 287–290 (2017).
20. Wu, S. F. et al. Observation of the quantum spin Hall effect up to 100 kelvin in a monolayer crystal. *Science* **359**, 76–79 (2018).
21. Tang, S. J. et al. Quantum spin Hall state in monolayer $1T'$ -WTe₂. *Nat. Phys.* **13**, 683–687 (2017).
22. Fei, Z. Y. et al. Edge conduction in monolayer WTe₂. *Nat. Phys.* **13**, 677–682 (2017).
23. Xu, Y., Gan, Z. X. & Zhang, S. C. Enhanced thermoelectric performance and anomalous Seebeck effects in topological insulators. *Phys. Rev. Lett.* **112**, 226801 (2014).
24. Wu, S. C., Shan, G. C. & Yan, B. H. Prediction of near-room-temperature quantum anomalous Hall effect on honeycomb materials. *Phys. Rev. Lett.* **113**, 256401 (2014).
25. Wang, J., Xu, Y. & Zhang, S. C. Two-dimensional time-reversal-invariant topological superconductivity in a doped quantum spin-Hall insulator. *Phys. Rev. B* **90**, 054503 (2014).
26. Gou, J. et al. Strain-induced band engineering in monolayer stanene on Sb(111). *Phys. Rev. Mater.* **1**, 054004 (2017).
27. Zang, Y. Y. et al. Realizing an epitaxial decorated stanene with an insulating bandgap. *Adv. Funct. Mater.* **28**, 1802723 (2018).
28. Song, Y. H. et al. High-buckled R3 stanene with topologically nontrivial energy gap. Preprint at <https://arxiv.org/abs/1707.08657> (2017).
29. Xu, C.-Z. et al. Gapped electronic structure of epitaxial stanene on InSb(111). *Phys. Rev. B* **97**, 035122 (2018).
30. Yuhara, J. et al. Large area planar stanene epitaxially grown on Ag(111). *2D Mater.* **5**, 025002 (2018).
31. Liao, M. H. et al. Superconductivity in few-layer stanene. *Nat. Phys.* **14**, 344–348 (2018).
32. Zhou, M. et al. Epitaxial growth of large-gap quantum spin Hall insulator on semiconductor surface. *Proc. Natl Acad. Sci. USA* **111**, 14378–14381 (2014).
33. Zhang, G. F., Li, Y. & Wu, C. J. Honeycomb lattice with multiorbital structure: Topological and quantum anomalous Hall insulators with large gaps. *Phys. Rev. B* **90**, 075114 (2014).
34. Wu, C. J., Bergman, D., Balents, L. & Sarma, S. D. Flat bands and Wigner crystallization in the honeycomb optical lattice. *Phys. Rev. Lett.* **99**, 070401 (2007).
35. Yan, B. H. et al. Topological states on the gold surface. *Nat. Commun.* **6**, 10167 (2015).
36. Son, Y. W., Cohen, M. L. & Louie, S. G. Half-metallic graphene nanoribbons. *Nature* **444**, 347–349 (2006).
37. Yazyev, O. V. & Helm, L. Defect-induced magnetism in graphene. *Phys. Rev. B* **75**, 125408 (2007).
38. Lahiri, J., Lin, Y., Bozkurt, P., Oleynik, I. I. & Batzill, M. An extended defect in graphene as a metallic wire. *Nat. Nanotech.* **5**, 326–329 (2010).
39. Huang, P. Y. et al. Grains and grain boundaries in single-layer graphene atomic patchwork quilts. *Nature* **469**, 389–392 (2011).
40. Ma, C. X. et al. Evidence of van Hove singularities in ordered grain boundaries of graphene. *Phys. Rev. Lett.* **112**, 226802 (2014).
41. Tao, L. et al. Silicene field-effect transistors operating at room temperature. *Nat. Nanotech.* **10**, 227–231 (2015).

Acknowledgements

This work was supported by the National Key R&D Program of China (grants nos 2016YFA0200603, 2017YFA0205004, 2018YFA0305603, 2016YFA0301001, 2018YFA0307100), the 'Strategic Priority Research Program' of CAS (XDB01020100), the National Natural Science Foundation of China (grants nos 91321309, 51132007, 21421063, 21473174, 21273210, 51788104), and the Fundamental Research Funds for the Central Universities (WK2060190084, WK234000065). A.Z. acknowledges a fellowship from the Youth Innovation Promotion Association of CAS (2011322). Y.X. acknowledges support from the Tsinghua University Initiative Scientific Research Program and the National Thousand-Young-Talents Program. The calculations were done on the 'Explorer 100' cluster system of Tsinghua University and on the 'Tianhe-2' of the National Supercomputer Computer Center in Guangzhou. W.D. acknowledge support from the National Natural Science Foundation of China (grants nos 11674188 and 11334006), and the Beijing Advanced Innovation Center for Future Chip (ICFC). S.-C.Z. is supported by the US Department of Energy, Office of Basic Energy Sciences, Division of Materials Sciences and Engineering under Contract No. DE-AC02-76SF00515.

Author contributions

A.Z., Y.X., B.W., W.D., S.-C.Z. and J.G.H. devised the experiments and provided financial and other support for the experiments and calculations. J.D. H.S. and X.Z. performed the MBE growth and STM/STS measurements. B.X., H.C., B.L. and Y.X. performed theoretical calculations. X.M. and J.D. performed the ARPES measurements. A.Z., Y.X., B.W., W.D., S.-C.Z. and J.G.H. analysed the data. A.Z. and Y.X. wrote the paper with input from other co-authors.

Competing interests

The authors declare no competing interests.

Additional information

Supplementary information is available for this paper at <https://doi.org/10.1038/s41563-018-0203-5>.

Correspondence and requests for materials should be addressed to A.Z. or Y.X. or B.W.

Methods

Stanene synthesis, STM and ARPES measurements. The synthesis of stanene was achieved by depositing Sn atoms on Cu(111) in ultrahigh vacuum with a base pressure of 1.3×10^{-10} mbar. Two polished Cu(111) single crystals from MaTeck GmbH and MTI Corporation were used in this work and gave the same results. The Cu(111) substrates were cleaned by cycles of Ar⁺ ion sputtering and annealing. Sn was evaporated from an alumina crucible heated to about 800 °C in an effusion cell (Quantech). The vacuum pressure was lower than 5×10^{-10} mbar during deposition and the deposition rate was controlled at 0.1–0.5 ML min⁻¹. Here 1 ML refers to the atomic density of the ultraflat stanene. During the deposition, the Cu single crystals were kept at a low temperature of 200 K. This substrate temperature was intentionally selected to ensure the growth of high-quality highly strained ultraflat stanene. Higher substrate temperatures will lead to the growth of buckled stanene with a much smaller lattice constant (Supplementary Fig. 9). The growth of stanene was characterized by low-temperature STM (Omicron GmbH) with a base pressure of 3×10^{-11} mbar. A tungsten tip was used and was intentionally dipped into the Cu(111) surface before STM and STS measurements to guarantee the cleanliness of the tip apex. The STS measurements were acquired simultaneously with *I*–*V* spectroscopy and topographic microscopy using a lock-in amplifier by applying a small sinusoidal modulation to the sample bias voltage (8 mV, 731 Hz). The correctness of STS was verified by checking the standard *dI/dV* spectrum of Cu(111) with the same tip. All STM and STS experiments were obtained at 5 K. For ARPES measurements, the stanene sample was prepared in situ on the cold Cu(111) substrate (~200 K) and investigated with ARPES spectra without any other transportation (during measurement the sample was kept at ~100 K). ARPES measurements were performed with 21.21 eV He I α rays using a Scienta DA30L analyser with a base pressure better than 1.5×10^{-10} mbar. The energy resolution was better than 5 meV and the angular resolution was better than 1% of the BZ.

First-principles calculations. Density functional theory calculations were performed with the Vienna ab initio simulation package⁴², using a projector-augmented-wave potential⁴³, the Perdew–Burke–Ernzerhof exchange–correlation

functional⁴⁴ and a plane wave basis with an energy cutoff of 300 eV. The surface lattice constant of Cu(111) was fixed to the experimental value of 2.56 Å. The Cu(111) surface was modelled by a periodic slab of six atomic layers, with the bottom three layers fixed during relaxation. Stanene on Cu(111) was studied by using a vacuum layer of ~15 Å, a $12 \times 12 \times 1$ Monkhorst–Pack *k*-point grid and Gaussian smearing with a broadening of 0.1 eV. The SOC was included in the self-consistent calculations of the electronic structure. The maximally localized Wannier functions were obtained from first-principles electronic structures by the WANNIER90 code⁴⁵. The edge states of semi-infinite stanene/Cu(111) were then computed using the software package WannierTools⁴⁶, where the Cu(111) substrate was simulated by a three-layer slab to reduce computational costs. Note that the topological gap is centred at approximately –0.91 eV for a three-layer slab; slightly higher in energy than that obtained for a six-layer slab (approximately –1.02 eV).

Data availability

The data that support the findings of this study are available from the corresponding authors upon reasonable request.

References

42. Kresse, G. & Furthmüller, J. Efficient iterative schemes for ab initio total-energy calculations using a plane-wave basis set. *Phys. Rev. B* **54**, 11169 (1996).
43. Blöchl, P. E. Projector augmented-wave method. *Phys. Rev. B* **50**, 17953 (1994).
44. Perdew, J. P., Burke, K. & Ernzerhof, M. Generalized gradient approximation made simple. *Phys. Rev. Lett.* **77**, 3865–3868 (1996).
45. Mostofi, A. A. et al. wannier90: A tool for obtaining maximally-localised Wannier functions. *Comput. Phys. Commun.* **178**, 685–699 (2008).
46. Wu, Q. S., Zhang, S. N., Song, H.-F., Troyer, M. & Soluyanov, A. A. Wannier Tools: An open-source software package for novel topological materials. *Comput. Phys. Commun.* **224**, 4059–4416 (2018).